Stability, reconstruction, and electronic properties of diamond (100) and (111) surfaces

Th. Frauenheim, U. Stephan, P. Blaudeck, and D. Porezag
Department of Physics, Technical University of Chemnitz-Zwickau, D-09009 Chemnitz, PSF 964, Germany

H.-G. Busmann
Fraunhofer Institut für Angewandte Materialforschung, D-28777 Bremen, Lesumer-Heerstrasse, Germany

W. Zimmermann-Edling
Freiburger Materialforschungsinstitut der Universität, D-79104 Freiburg, Stefan-Meier-Strasse 31a, Germany and Institut für Physik, Universität Basel, CH-4056 Basel, Switzerland

S. Lauer
Freiburger Materialforschungsinstitut der Universität, D-79104 Freiburg, Stefan-Meier-Strasse 31a, Germany
(Received 20 May 1993; revised manuscript received 23 August 1993)

Results of scanning-tunneling-microscopy (STM) and molecular-dynamics (MD) annealing studies based on quantum-mechanically derived interatomic forces using a *semiempirical* density-functional approach are combined for analyzing diamond surface structures. Experimentally obtained STM images of diamond (100) and (111) faces on polycrystalline films reveal (1×1), $(\sqrt{3}\times\sqrt{3})R30°$, and possible (2×1) structures. The (100) faces show stable (2×1) reconstruction with dimer formation. Surface structures with and without adsorbed hydrogen are determined and their stability is obtained by MD simulated annealing techniques. The bulklike and $(\sqrt{3}\times\sqrt{3})R30°$ structures, as they are observed on grown (111) facets, are attributed to the two different single atomic (111) layers, which support growth mechanisms, in which the two alternating single atomic layers grow in turn and not simultaneously. The equilibrium surface modifications which have been realized are electronically characterized by investigating the local electronic density of states at selected surface atoms. This information is compared and related to the features seen in the STM images.

I. INTRODUCTION

Diamond vapor growth is stimulating a still increasing number of research activities. It opens new perspectives in thin film science and technology due to the extreme mechanical, optical, and electronic properties of diamond. Since being introduced to the wider scientific community more than ten years ago,[1,2] much information has been gained on how to prepare high quality films.[3–6] Although many current activities are focused on obtaining knowledge about molecular growth mechanisms,[4,7–12] the growth and preparation of diamond surfaces with well defined molecular and electronical properties via an atomically controlled diamond vapor deposition is only beginning.

Experimental and theoretical methods, which will contribute to this ultimate goal, are *in situ* characteristics of growing thin films, atomic scale imaging, and molecular-dynamics simulations. Current simulated annealing (SA) techniques performed by molecular-dynamics (MD) calculations[13–15] are an approach well suited and simultaneously efficient enough (1) to test the stability of given molecular structures, (2) to evaluate new structures, (3) to study possible pathways of transitions between different structures, and (4) to follow chemical reactions between hydrogen, carbon, and hydrocarbon species with predetermined diamond surface structures. Furthermore, the local electronic density of states (LDOS) may be obtained. SA-MD calculations are therefore well suited to interpret atomic-scale images of diamond surfaces, which provide a fundamental insight into growth mechanisms on a molecular level. When temperatures typical for the substrate in diamond vapor growth are used, a realistic simulation of individual molecular growth mechanisms is possible.

All MD simulations that have been steadily developed for applications to chemical reactions on solid surfaces[13,16–19] are based on the assumption of an accurate calculation of the total energy as a function of all atomic coordinates. The gradients of the total energy, evaluated at the given atom positions, yield the interatomic forces. Within these simulations the Newtonian equations of motion for all atoms within the structural configuration are integrated numerically, and stable or metastable configurations (corresponding to global or local minimizations of the energy) are adjusted deterministically at finite temperature.

Various theoretical concepts are currently applied for total energy calculations of atomic carbon structures. Classical concepts are based on the construction of *empirical* potentials,[13] and quantum-mechanical concepts make use either of *semiempirical* quantum potentials[11,14] or of *self-consistent* calculations performed on an *ab initio* level within the Hartree-Fock (HF) and density-functional (DF) theory.[20] In most previous studies, the interatomic forces are derived from empirical potentials,

which are fitted either to experimental data[21,22] or to results of *ab initio* quantum chemical calculations.[18] This offers computational speed and is most successful when physical properties of well understood crystalline and amorphous bulk materials are studied. However, geometries and chemical bonding characteristics calculated for finite clusters and molecules are not realistic,[23,24] which is also true for exploratory investigations at surfaces, where one is interested in testing unknown reactions, rearrangements, and transition states which are far from equilibrium configurations. Insensitive growth modeling of crystalline substrate surfaces has shown that additional constraints, which demand the correct reproduction of microclusters, molecules, and surfaces, increase the number of parameters for a unique fit of the *empirical* potentials to a point that an analytical representation is extremely difficult if possible at all. The problems inherent to the usage of *empirical* potentials in MD simulations increase further if different kinds of atoms are involved, such as carbon and hydrogen. However, just this situation is realized in diamond vapor growth.

Most investigations of growth conditions, based on an *ab initio*[25] or a *semiempirical*[26,27] quantum-mechanical origin, deal with the calculation of the total energy for the ground state surface configurations of given static atomic arrangements[28–31] including adsorbed CH species on crystalline surfaces.[11,32–34] The final structures of minimized energy are found by a geometric optimization using energy gradient methods. Such calculations provide information about stable geometries, corresponding binding energies, and quantitative information on the topology of potential energy surfaces. However, dynamic processes, which probe transition states, have not been considered.

Generalizations of these methods that attempt to investigate the dynamic properties of diamond surfaces under different saturation conditions and during the adsorption of molecular fragments are rare.[14,15] Iarlori *et al.*[20] recently investigated the reconstruction of the clean diamond (111) surface by a series of *first principles* MD calculations proving the stability of symmetric dimerized π-bonded Pandey chains on a clean (111) surface[35] up to 2500 K.

Due to the limitations in the transferability of empirical potentials and the use of time consuming *ab initio* DF-MD methods, approximate DF schemes for MD using minimal basis sets have been developed by us and others.[36–39] Compared to the self-consistent-field (SCF) methods, they allow for simulations of systems which are large enough to represent the energetic behavior of surfaces. At the same time, their results deviate only slightly from those of the more sophisticated methods. Thus an application of the approximate scheme, described below, to the problems of interest is justified.

In this paper, results of scanning tunneling microscopy (STM) and MD annealing studies based on quantum-mechanically derived interatomic forces are combined using a semiempirical density-functional (DF) approach. The paper is organized as follows. Section II presents a review of stable surface views of diamond (110) and (111) faces on polycrystalline films obtained by scanning tunneling microscopy. Section III outlines the semiempirical DF approach for the calculation of interatomic forces used in the MD simulations of Sec. IV to obtain the structure and stability of diamond (100) and (111) faces. In Sec. V the local electronic surface densities of states are calculated at selected atom sites for different stable surfaces. Concluding, the theoretical results are related to atomic-scale images obtained by STM in Sec. VI, which is a first major step towards an atomically controlled preparation of diamond surfaces.

II. SCANNING TUNNELING MICROSCOPY

Polycrystalline diamond films were grown by hot-filament vapor deposition as described elsewhere.[40,41] The quality and morphology of the films is quite reproducible, mainly judged by Raman spectroscopy, x-ray diffraction analysis, and scanning electron microscopy. Details of the deposition process and of the STM measurements (performed by a Digital Instruments Nanoscope II at room temperature in air) can be found in Ref. 42.

When STM is applied to polycrystalline films, it is highly desirable that the facets of interest be oriented almost parallel to the substrate surface. If the morphology of the films were to be determined only by the growth form (shape of the crystallities in the initial deposition process) and the principal of evolutionary selection, then films of octahedral and cubic growth forms would be best suited to study (100) and (111) faces, respectively. At the same time, it would be extremely difficult to visualize (100) facets of films of cubo-octahedral or cubic growth form, and to visualize (111) facets of films of cubo-octahedral or octahedral growth form. However, 110-texture formation induced by twin formation and possibly other mechanisms renders possible the application of STM to (100) and (111) facets of films of quite different growth forms.

100-textured films of octahedral growth form were deposited at a substrate temperature of 750 °C, a gas mixture of 1 mol % CH_4 in H_2, a flow rate of 50 SCCM (SCCM denotes cubic centimeter per minute at STP) and a pressure of 70 Torr. Scanning electron microscopy (SEM) and STM images of 12-μm-thick films show the expected (100) facets oriented almost parallel to the surface. However, neither STM analysis of these nor of microwave deposited 100-textured films[44] has revealed images from which the atomic structure of the surface could have been deduced.

STM images of films of well defined structure on the atomic scale have been obtained from films of cubo-octahedral and cubic growth form. Some of the films were deposited with a pulsed high pressure valve for gas inlet, which greatly enhances the twin formation rate during growth.[41] It is important for the context here that this pulsed gas inlet does not change either the growth form or the macroscopic growth rate, which clearly shows that the growth rate of the (100) and (111) facets is not influenced by this gas inlet. The structure formation on the facets is controlled by the gas composition, the total averaged gas flow rate, the pressure, the substrate

temperature, and the reactor design.

Other films, even those of a cubic growth form, have been obtained in our reactor at a substrate temperature of 1000 °C, a flow rate of 50 SCCM and a pressure of 40 mbar using a gas mixture of 0.5 mol % CH_4 in H_2. However, the (111) facets are strongly twinned and 110-texture formation evolves at the expense of the expected 111 texture. This effect could have been strongly reduced by using a constant driven supersonic valve for the gas inlet. Some details of this experimental setup are described elsewhere.[43] A cubic growth form with much lower twin formation on the developing (111) facets is obtained. The characteristic parameters for this were found at a valve temperature of about 950 °C, a gas mixture of 1 mol % CH_4 in H_2, a flow rate of 30 SCCM, a pressure of 50 mbar, and a substrate temperature of 925 °C. A film of 8 μm thickness obtained in this way shows 111 texture with (111) facets, which are aligned almost parallel to the surface. We note that the growth form obtained under such conditions but using a normal gas inlet has much stronger cubo-octahedral character than the films grown with the hot value. In the following, STM images of films of cubo-octahedral and cubic growth form are presented.

A. (100) surface structure

Figure 1 shows an STM image of cubo-octahedral growth form. Rows are visible which are formed due to the (2×1) surface reconstruction.[42,45] The rows appear in two directions which are perpendicular to each other. The height difference between two adjacent layers of rows of different orientation has been determined to be 0.11 nm, proving that the individual steps are of single atomic layer height. Two types of steps are visible, which according to Chadi's notation[46] are known as S_A steps and S_B steps if the direction of the upper layer rows is parallel or normal to the step direction, respectively. Both kinds of steps are rough. Asymmetric sets of rows are visible. In the case of S_A steps, they extend onto the layer underneath, and in the case of S_B steps, they are oriented parallel to the upper rows. Similar structures are commonly observed on (100) surfaces of Si and Ge films, where they are attributed to growth processes. In these cases, it is well known that growth proceeds with the (2×1) reconstruction, which together with other observations[45] provide very strong evidence that the 100 faces investigated here also grew with the (2×1) reconstruction.

Independent of whether the surfaces grew with the observed structure or not, such atomically flat faces are of considerable interest when one attempts to deduce well defined electrochemical properties of the diamond surfaces. Possible atomic structures and the corresponding electronic densities of states are discussed below.

The fact that the (100) faces of 100-textured films do not show such flat faces or any atomically resolved structures gives first evidence of an influence of the growth conditions on the structures seen. This is further supported by the images obtained from the 111-textured films. Figure 2 shows a STM image of a (100) face, where again a (2×1) surface reconstruction is visible. However, the individual dimers within the rows are now resolved. Any attempt to get a structure within the rows of the 110-textured films failed. Thus we consider differences of the structures seen in Figs. 1 and 2 as being due to different electronic and hence atomic structure.

B. (111) surface structure

Figure 3 shows a STM image of a (111) face of the 110-textured film.[42] A sixfold symmetry is visible, with a characteristic spot-spot distance of 0.25 nm corresponding to a (1×1) structure. On the same films, sometimes even on the same facet, quite different structures are visible as it is shown in Fig. 4. Rows appear with a row-row distance of 0.21 nm. Three different directions of the rows are observable, which are rotated against each other by 120°. This distance and angular behavior are consistent with Pandey's (2×1) chain model.[20,35] A third

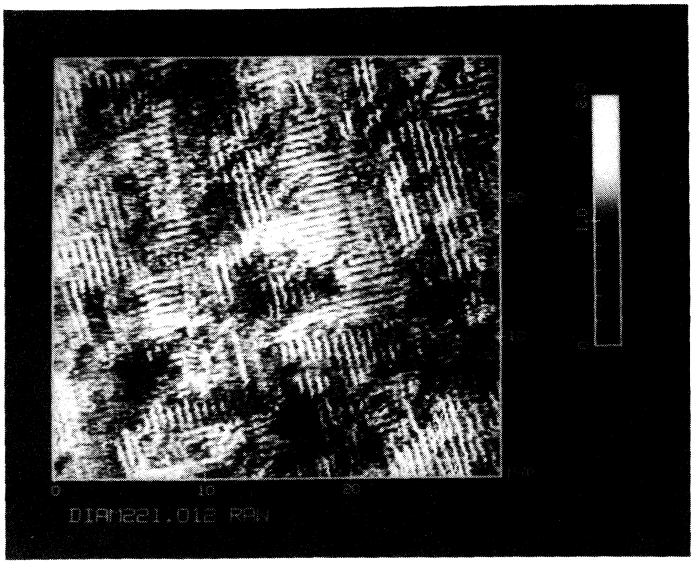

FIG. 1. Image of a (100) facet of a polycrystalline diamond film obtained with a scanning tunneling microscope. Deposition parameters: 1 mol % CH_4 in H_2, substrate temperature equals 925 °C, continuous accelerated beam for gas inlet (Ref. 43), diameter of orifice equals 20 μm, stagnation pressure behind the nozzle equals 6 bars, temperature of the nozzle equals 500 °C, gas flow equals 22 SCCM, pressure in the chamber equals 50 mbar. Tunneling parameters: constant height mode, $I_t = -1.0$ nA, $U_t = -183$ mV.

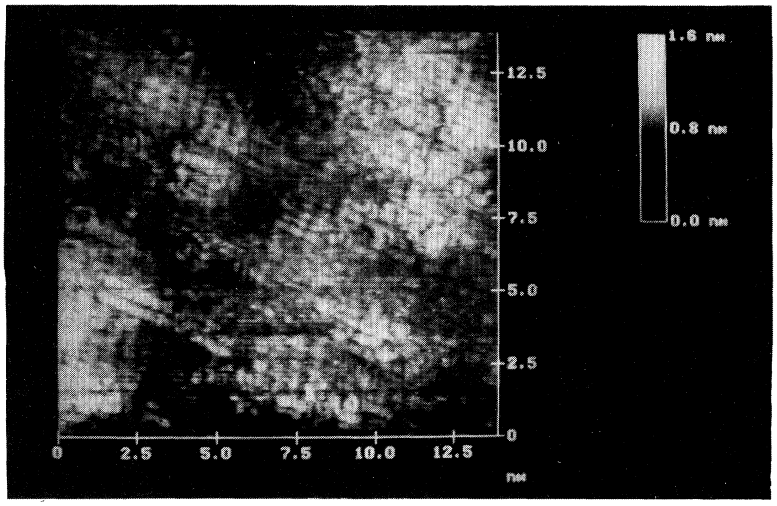

FIG. 2. Image of a (100) facet of a polycrystalline diamond film obtained with a scanning tunneling microscope. Deposition parameters: 1 mol% CH_4 in H_2, substrate temperature equals 925 °C, continuous accelerated beam for gas inlet, diameter of orifice equals 30 μm, stagnation pressure behind the nozzle equals 1.5 bars, temperature of the nozzle equals 950 °C, gas flow equals 30 SCCM, pressure in the chamber equals 50 mbar. Tunneling parameters: constant height mode, $I_t = -1.7$ nA, $U_t = 400$ mV.

structure on these (111) facets is visible in the lower, right part of Fig. 4. This structure exhibits bright elongated dots, where the shorter dot-dot distance is 0.25 nm and the longer 0.36 nm.

In the case of the 111-textured film, structures such as those described above are observed as well as a fourth structure. Figure 5 shows an image where broad spots are arranged in a hexagonal pattern with a characteristic spot-spot distance of 0.44 nm. This structure has been assigned to the $(\sqrt{3}\times\sqrt{3})$ $R30°$ hexagonal surface cell reconstruction,[43] which under various conditions was found to be stable on other semiconductor surfaces too.[47,48]

Altogether, four different structures have been observed on the diamond (111) surface. This variety of structures might give evidence that vapor growth of diamond (111) faces is due to multifarious molecular mechanisms. This is supported by STM images such as those shown in Fig. 6, where three of the four structures are visible on an area of 20 nm by 20 nm. Much more information than the spacings and orientations obtained from the STM images is necessary to come finally to a complete description of the molecular structure and eventually of possible growth mechanisms of this structure. The calculations described below, which yield realistic molecular structures and corresponding electronic state densities, are an important step in this direction.

III. SEMIEMPIRICAL MD-DF APPROACH

Via MD-SA the atoms of the initial structure configuration (substrate and hydrocarbon fragments) move, within the Born-Oppenheimer approximation, on the potential energy surface until they evolve to the structure of minimal energy. The interatomic forces are calculated within a semiempirical MD-DF approach originally introduced by Seifert, Eschring, and Biegert for cluster calculations,[36,38] which we will briefly summarize here.

For the initial step, effective one-electron potentials

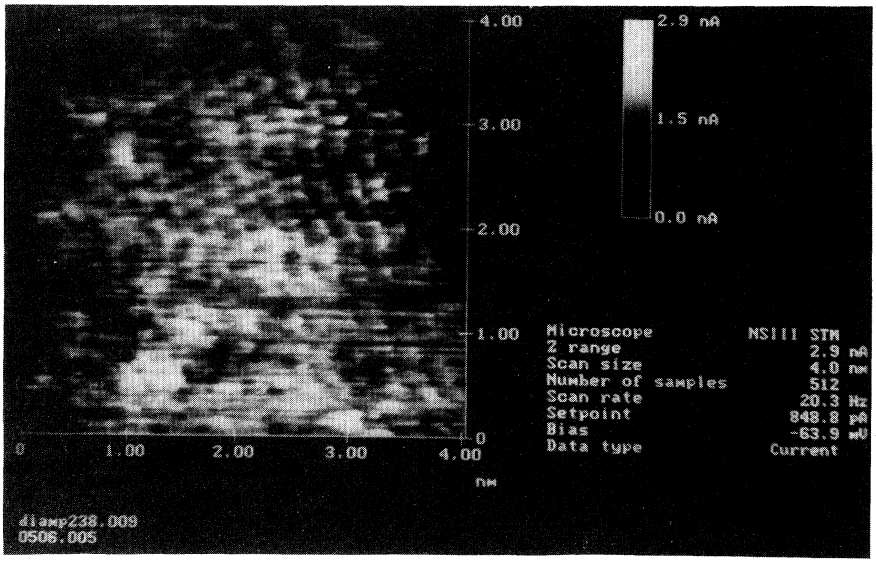

FIG. 3. Image of a (111) facet of a polycrystalline diamond film obtained with a scanning tunneling microscope. The deposition parameters are the same as those for the film of Fig. 2. Tunneling parameters: constant current mode, $I_t = 0.85$ nA, $U_t = -64$ mV.

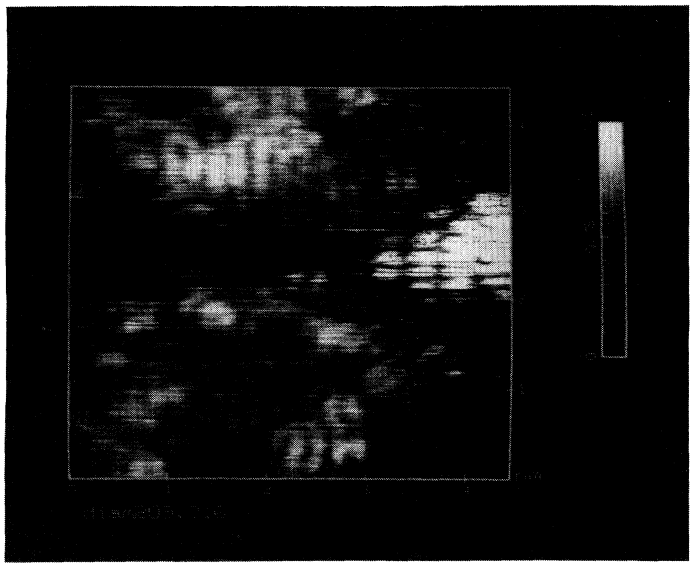

FIG. 4. Image of a (111) facet of a polycrystalline diamond film obtained with a scanning tunneling microscope. Deposition paramers: 1 mol % CH_4 in H_2, substrate temperature equals 925 °C, pulsed accelerated beam for gas inlet (Ref. 41), stagnation pressure behind the nozzle equals 1.5 bars, temperature of the nozzle is RT, averaged gas flow equals 75 SCCM, background pressure in the chamber equals 50 mbar. Tunneling parameters: constant current mode, $I_t = 1.3$ nA, $U_t = 574$ mV.

and the corresponding electronic wave functions of the single atoms are determined in a *nonrelativistic* and *self-consistent* way in the *local density approximation* (LDA) using the local exchange and correlation potential of Hedin and Lundquist.[49]

The resulting single-atom valence electron wave functions φ_μ of s and p symmetry are placed at all atomic positions $\mathbf{R}_l$ and now form the minimal basis for a linear combination of atomic orbitals (LCAO) ansatz for a representation of the Kohn-Sham orbitals of the system.

$$\psi(\mathbf{r}) = \sum_\mu c_\mu \varphi_\mu(\mathbf{r} - \mathbf{R}_l) \ . \tag{1}$$

In this way the Kohn-Sham equations are transformed into a set of algebraic equations *(secular equations)* which are solved *non-self-consistently* by diagonalization of the secular matrix,

$$\sum_\mu c_\mu^i (h_{\mu\nu} - \varepsilon_i S_{\mu\nu}) = 0 \ , \tag{2}$$

yielding the cluster orbital energies and the corresponding eigenfunctions. The $h_{\mu\nu}$ are the Hamiltonian matrix elements of the basis functions with the Kohn-Sham Hamiltonian:

$$\hat{h} = \hat{t} + V_{\text{eff}}(\mathbf{r}) \ , \tag{3}$$

where $\hat{t}$ is the operator of kinetic energy, and V_{eff} is the effective one-particle potential, consisting of the electron-nuclear part V_{ext}, the mean-field electron-electron interaction contribution (Hartree potential) V_H, and the exchange-correlation part V_{xc} in the LDA:

$$V_{\text{eff}} = V_{\text{ext}} + V_H + V_{\text{xc}} \ . \tag{4}$$

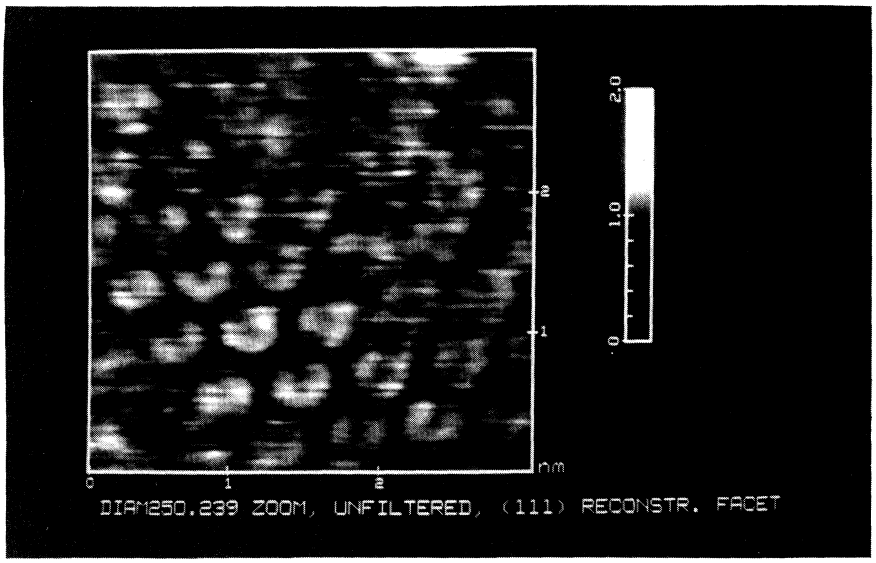

FIG. 5. Image of a (111) facet of a polycrystalline diamond film obtained with a scanning tunneling microscope. The deposition parameters are the same as those for the film of Fig. 2. Tunneling parameters: constant current mode, $I_t = 0.5$ nA, $U_t = -48$ mV.

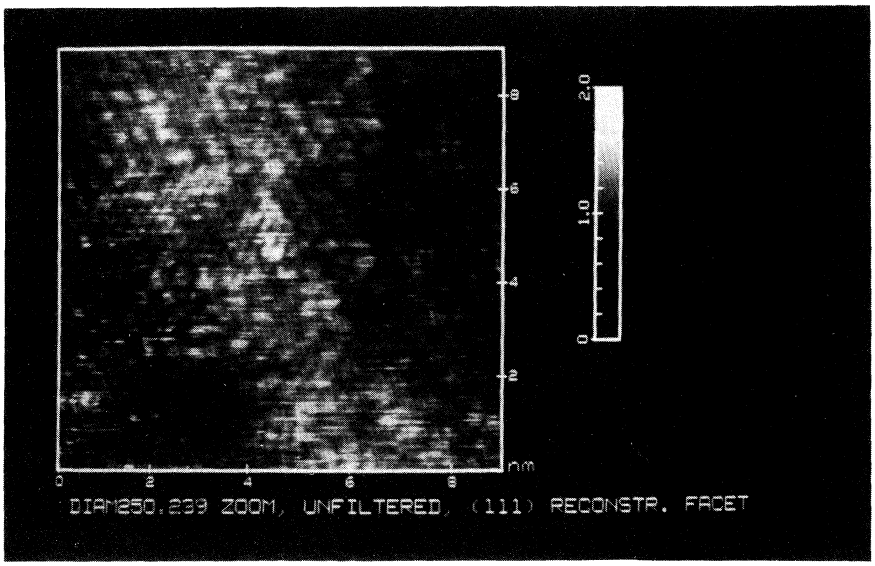

FIG. 6. Image of a (111) facet of a polycrystalline diamond film obtained with a scanning tunneling microscope. The deposition parameters are the same as those for the film of Fig. 2. Tunneling parameters: constant current mode, $I_t = -0.5$ nA, $U_t = -48$ mV.

The overlap matrix elements $S_{\mu\nu}$ are due to the nonorthogonality of the basis functions at different atom sites. As an approximation we write V_{eff} as a sum of potentials V_l^0 of neutral atoms:

$$V_{\text{eff}} = \sum_l V_l^0 \ . \tag{5}$$

Consistent with this approximation, one can neglect several contributions to the Hamiltonian matrix elements $h_{\mu\nu}$:[36,50]

$$h_{\mu\nu} = \begin{cases} \langle \varphi_\mu | t + V_l + V_k | \varphi_\nu \rangle & \text{if } \mu \cap \nu \in \{l,k\} \\ 0 \quad \text{otherwise} \ . \end{cases} \tag{6}$$

This treatment may be viewed as the LCAO variant of a cellular Wigner-Seitz method, as applied to molecules by Inglesfield.[51]

As shown by other authors[52,53] and by our own results[38] the cohesive energy of the structure can be written as a sum of two parts:

$$E_{\text{tot}}(\{\mathbf{R}_l\}) = E_{\text{bind}}(\{\mathbf{R}_l\}) + E_{\text{rep}}(\{\mathbf{R}_l - \mathbf{R}_k\}) \tag{7}$$

$$= \sum_i n_i \varepsilon_i(\{\mathbf{R}_l\}) + \sum_l \sum_{<k} V_{\text{rep}}(\{\mathbf{R}_l - \mathbf{R}_k\}) \ . \tag{8}$$

The first term represents the so-called band structure energy, determined by the summation over all occupied cluster orbital energies ε_i (occupation number n_i), which takes into account the intra-atomic electron-electron interaction through the *self-consistent* LDA calculation of the single-atom valence electron orbitals.

The second term E_{rep} consists of a short-range repulsive energy, which includes the partly compensating contributions of the electrostatic core-core interaction, and the interaction between electrons at different lattice sites.

An accurate quantum-mechanical calculation of the repulsive term is computationally very time consuming and requires a much more extended basis. Such a description would make applications of this method to the relative large systems (of interest here) practically impossible. Therefore the repulsive energy contribution is fitted by an *empirical* repulsive short-range two-body potential V_{rep} as polyomial of fifth order in such a way that the potential energy curves of the relevant two-atom molecules are reproduced in relation to the force calculations for the MD simulation over a wide range of interatomic separations.

On the basis of the total energy calculation of the structure as a function of all atomic coordinates the interatomic forces can be calculated from the gradients of the total energy at all atom sites using a modification of the Hellmann-Feynman theorem.

$$\mathbf{F}_l = -\frac{\partial E_{\text{tot}}}{\partial \mathbf{R}_l} = \sum_i n_i \sum_\mu \sum_\nu c_\mu^i c_\nu^i \left[-\frac{\partial h_{\mu\nu}}{\partial \mathbf{R}_l} + \varepsilon_i \frac{\partial S_{\mu\nu}}{\partial \mathbf{R}_l} \right] - \frac{\partial E_{\text{rep}}}{\partial \mathbf{R}_l} \ . \tag{9}$$

In testing and characterizing the method, it has proven to be complex enough to model the following well-known carbon and hydrocarbon structures: carbon microclusters $C_n (n < 20)$; hydrocarbon molecules, e.g., CH_4, C_2H_2, C_2H_4, C_2H_6, C_6H_6, C_6H_{12}; fullerenes, e.g., C_{60}; bulk crystalline diamond and graphite; bulk amorphous *a*-C and *a*-C:H. The results show that for the systems above, one obtains quantitatively correct bond length and bond angles for equilibrium geometries. Further, the structural statistics for amorphous materials and the relative differences of the cohesive energy as a function of structure and coordination are reproduced as well.[15,38]

The method includes the most relevant interaction mechanisms for a correct estimation of angular dependent attractive and repulsive interatomic forces in the cases of undercoordination and overcoordination, respectively, during the MD structure simulation process. As an important requirement it accounts very well for the π-bonding effects which are characteristic in the carbon chemistry.

This justifies applications of real temperature dynamical structure simulations for the study of the stability and reconstruction of the (100) and (111) diamond surfaces under variation of the saturation by hydrogen and the elementary reaction mechanisms for the adsorption of hydrocarbon molecules or fragments onto this surface.

IV. DYNAMIC ANNEALING INVESTIGATIONS

The surface stability of (100) and (111) diamond was studied by using two-dimensional periodic eight-layer-thick slab supercell arrangements with 128 and 96 C atoms, respectively. The bottom face of the slab has been saturated by hydrogen to tie off the dangling orbitals, while stability and dynamic restructuring are studied on the other face, fixing the bottom carbon layer atoms in their original positions to simulate the effect of an infinite crystal substrate. The initial atomic coordinates correspond to bulk (1×1) structures or to the atomic arrangements of unreconstructed as well as reconstructed surfaces with varying degree of surface saturation. Small random initial velocities for the thermal atomic vibrations in the top carbon layers are applied to simulate the effect of finite kinetic lattice temperature. The Verlet algorithm[54] has been applied for the integration of Newton's equations for all atoms in the structure to follow the atom trajectories in time:

$$M_I\ddot{\mathbf{R}}_I=-\partial E/\partial\mathbf{R}_I\ . \tag{10}$$

Including the carbon-hydrogen interaction a time step of 20 atu (1 atu$=2.4\times10^{-17}$ sec) has been found to be sufficient for handling these equations and to guarantee the conservation of energy during the simulation run. The time evolution of the surface slab systems in the clean configurations and upon adsorption of different monolayers is then simulated to study the stability and dynamic restructuring of the surface atoms and the adsorbed monolayers.

A. (100) surface stability

At first we investigated the stability of the clean unreconstructed (100) surface. This surface under MD annealing conditions was found to be highly unstable and prefers to relax to a symmetric dimerized geometry. The resulting surface is stabilized by a strong π-bonded dimer chain. As a result, a stable (2×1) reconstruction, shown in Fig. 7 (panel 1), is formed, yielding a gain in binding energy of 1.5 eV per surface site, which are indicated as sites that have radical electrons in the unreconstructed bulk positions. Information about the structures of this and of all the following investigated surface modifications, e.g., bond length and angles as well as the s character of chemical bonding, is summarized in Table I. The atom numbers in brackets correspond to the atom numbers in the panels of Figs. 7, 8, and 10.

In a next simulation step, we show that the presence of thermal hydrogen atoms or molecules near the surface leads to the reaction of the π-bonded dimer chains and produces C-H bonds. For atomic hydrogen, reactions occur at all temperatures and positions. However, for molecular hydrogen, dissociation followed by a subsequent formation of C-H bonds is only observed if the molecules are located above the dimer bonds. The resulting surface maintains a stable (100)2×1:H reconstruction shown in Fig. 7 (panel 2), but with elongated surface C-C dimer bonds (compare values in Table I). This monohydrogenated surface under SA conditions of chemical vapor deposition (CVD) diamond growth of about 1200 K remains stable with respect to higher abundances of hydrogen atoms. This supports recent experimental findings obtained by low-energy electron diffraction

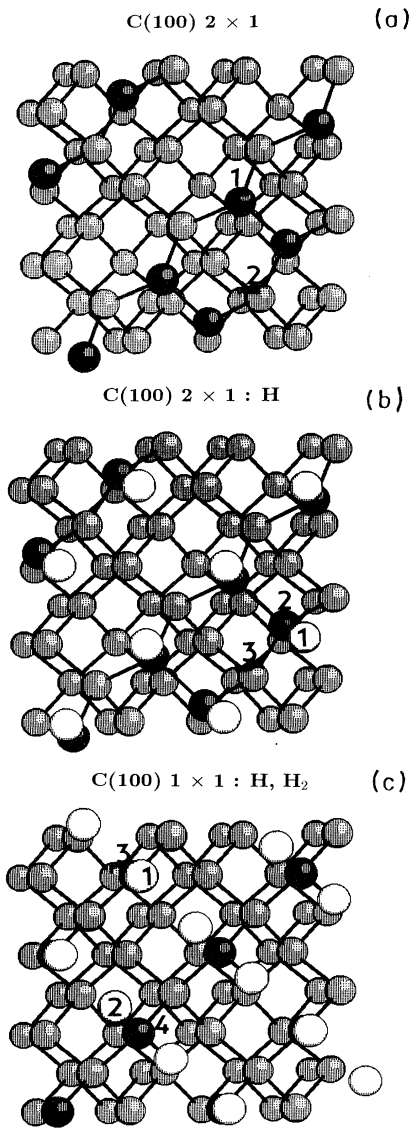

FIG. 7. Stable diamond (100) surface structures with variation of the saturation by hydrogen. (a), C(100)2×1; (b), C(100)2×1:H; (c) C(100)1×1:H, H_2. The atom numbers in the panels of this and the following figures are related to assignments of bond length and bond angle values given in Table I.

TABLE I. Quantitative values for equilibrium bond lengths, bond angles, and *s* character of bonding. The atom numbers correspond to the atom enumeration in Figs. 7, 8, and 10. If the same numbers occur in parentheses, different atoms of the same geometry are considered.

Surface structure	*d*, bond lengths (Å) (*b*: bulk)		*α*, bond angles (deg)		*s* character of selected orbitals (*f*: free)	
C(100)2×1	(1−1)=1.41	(1−2)=1.50	(1−1−2)=109	(2−1−2)=113.7	(1−1)=0.21	(1−2)=0.29
	(1−1)=1.41[a]	(1−1)=1.38[b]			(1−*f*)=0.22	
	(1−1)=1.43[c]	(1−1)=1.40[d]				
C(100)2×1: H	(1−2)=1.07	(2−2)=1.58	(1−2−3)=113	(1−2−2)=112	(2−1)=0.34	(2−2)=0.16
	(2−3)=1.54	(2−2)=1.73[e]	(2−2−3)=104		(2−3)=0.25	
	(2−2)=1.61[a]	(2−2)=1.56[b]				
	(2−2)=1.67[c]	(2−2)=1.64[f]				
	(2−2)=1.67[d]					
C(100)1×1: H,H_2	(1−3)=1.07	(2−4)=1.07	(2−4−2)=103	(1−3−*b*)=122	(3−*f*)=0.0	(3−1)=0.38
	(3−*b*)=1.48	(4−*b*)=1.52	(*b*−3−*b*)=116		(4−2)=0.26	
C(111)1×1: H	(1−2)=1.08	(2−3)=1.54	(1−2−3)=109.4		(2−1)=0.25	(2−3)=0.25
	(3−*b*)=1.54	(1−2)=1.13[g]				
C(11)2×1: H	(1−2)=1.09	(2−2)=1.56	(1−2−2)=104	(1−2−3)=105	(2−1)=0.17	(2−2)=0.22
(*P*):Pandey	(2−3)=1.55	(3−3)=1.57	(2−2−2)=107	(2−2−3)=118		
C(111)2×1 (*P*)	(1−1)=1.39	(1−2)=1.49	(1−1−2)=121	(1−1−3)=118	(1−2)=0.37	(1−*f*)=0.05
	(1−3)=1.49	(3−3)=1.54	(2−1−3)=114	(1−3−3)=121	(3−3)=0.25	
	(3−*b*)=1.57	(1−1)=1.44[h]	(3−3−3)=108	(1−3−*b*)=95		
C(111)2×1: H	(1−2)=1.06	(2−2)=1.54	(1−2−2)=114	(1−2−3)=115	(2−1)=0.34	(2−2)=0.24
(SC)	(2−3)=1.54	(2−2)=1.46[g]	(2−2−3)=108			
C(111)$\sqrt{3}\times\sqrt{3}$	(1−2)=1.44	(1−3)=1.56	(2−1−2)=94	(1−2−4)=98	(1−2)=0.07	(1−*f*)=0.14
	(2−4)=1.52		(2−1−3)=116	(1−3−5)=136	(1−3)=0.72	(2−1)=0.12
C(111)$\sqrt{3}\times\sqrt{3}$: H	(1−2)=1.05	(2−2)=1.57	(1−2−3)=1.24	(1−2−2)=1.21		
	(2−3)=1.51					

[a]Reference 13.
[b]Reference 29.
[c]Reference 31.
[d]Reference 39.
[e]Reference 11.
[f]Reference 33.
[g]Reference 30.
[h]Reference 20.

(LEED) upon heating the surface.[55] Because of steric overcrowding the dihydrogenated surface in either the ideal configuration of adsorbed H_2 or in the annealed twisted configuration becomes unstable and tends to expel H_2 molecules. This point has been recently discussed by Yany and D'Evelyn.[56] The most stable surface modification that we have obtained is the (1×1) alternating dihydrogenated, monohydrogenated surface structure (100)1×1:H,H_2, shown in Fig. 7 (panel 3).

B. (111) surface stability

Turning now to the (111) surface (for the local bonding properties, compare Table I), the (1×1) bulklike hydrogen terminated single dangling bond (1DB) surface, see panel 1 in Fig. 8, is found to be stable under SA conditions up to temperatures of 2000 K. Upon successive adsorption of C and CH groups at three neighboring 1DB surface atoms, a spontaneous reconstruction is observed under SA conditions, favoring a $(\sqrt{3}\times\sqrt{3})R30°(111)$ hexagonal surface cell which is stable at CVD diamond growth conditions of 1200 K. Two different locations of the trimer groups are found to be metastable in energy. Here the trimer groups are located either on the hollow sites of the sixfold rings (H site) or on top of an atom of the second layer underneath (T site). For an adsorbed C monolayer, a gain of binding energy is obtained by the formation of two bonds (1.54 Å equilibrium length) between the atoms of each top trimer C group, see Fig. 8 (panel 2), for the H site. However, CH adsorption causes further energy gain, where now fully saturated symmetric C trimers are formed with bonds between each pair of carbon atoms (1.54 Å length). The configuration for the more stable T-site trimer groups is shown in Fig. 8 (panel 3), compare also Table I. The passivating H atoms are at positions very similar to a nonreconstructed single dangling bond surface and should therefore have low energy. The energy differences between the T- and H-site structures are 0.159 eV and −0.58 eV per surface site for the C- and CH-adsorption layers, respectively. Thus a C layer favors the H-site configuration with a C(111)$\sqrt{3}\times\sqrt{3}$ surface, in contrast to the CH layer which prefers the T-site configuration with C(111)$\sqrt{3}\times\sqrt{3}$:H. These are presented as top views in Fig. 9. Slightly more stable structures have been obtained under SA conditions that start from a one-to-one adsorption of a complete C and CH monolayer stabilizing the (111)2×1 and (111)2×1:H single chain (SC) reconstruction, shown in Fig. 10 (panel 1) for the CH-adsorption case. The energy gain of the clean and hydrogenated (111)2×1 (SC) structures per surface site compared to the corresponding (111)$\sqrt{3}\times\sqrt{3}$ hexagonal surface cell reconstruction is

0.3 eV for the clean and 0.6 eV for the hydrogenated modification, respectively. An observation of the (111)2×1 (SC) structure beside the $\sqrt{3}\times\sqrt{3}$ hexagonal surface cell on the same as grown faces could be caused by two different growth processes or by different nucleation mechanisms when the growth is terminated. Furthermore, as the most stable (111) clean 1DB structure, the (2×1) reconstructed Pandey chain has been obtained (energy gain of 0.6 eV compared to a clean bulk surface) characterized by symmetric strongly π-bonded chains and structural data, given in Table I. The adsorption of hydrogen onto these chains causes the π bonds to break and form metastable C(111)2×1:H(P) Pandey chains, shown in Fig. 10 (panel 2), compare data in Table I. This configuration, which with an energy of 0.75 eV per surface site is less stable than the hydrogenated bulk (111)1×1:H surface, has proven to be stable under SA conditions up to 2500 K as already predicted by Iarlori *et al.*[20] However, the question regarding the reconstruction dynamics of this special configuration remains open.

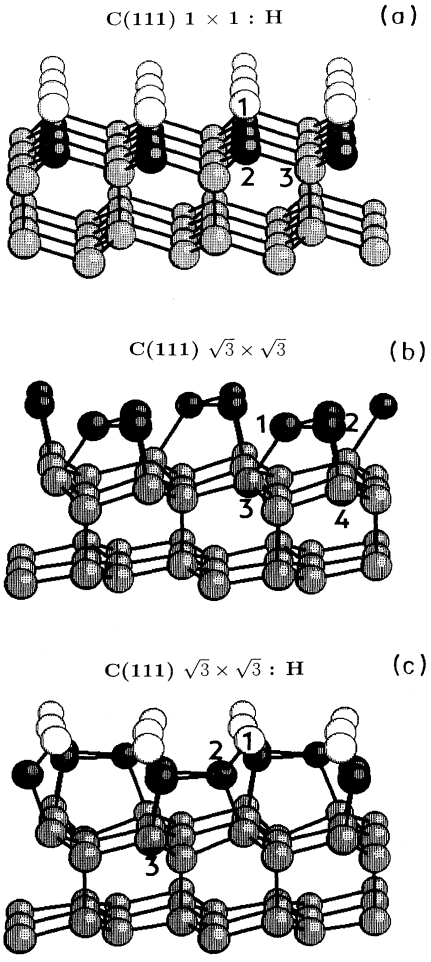

FIG. 8. Stable diamond (111) structures. (a), C(111)1×1:H; (b) C(111)$\sqrt{3}\times\sqrt{3}$; (c) C(111)$\sqrt{3}\times\sqrt{3}$:H.

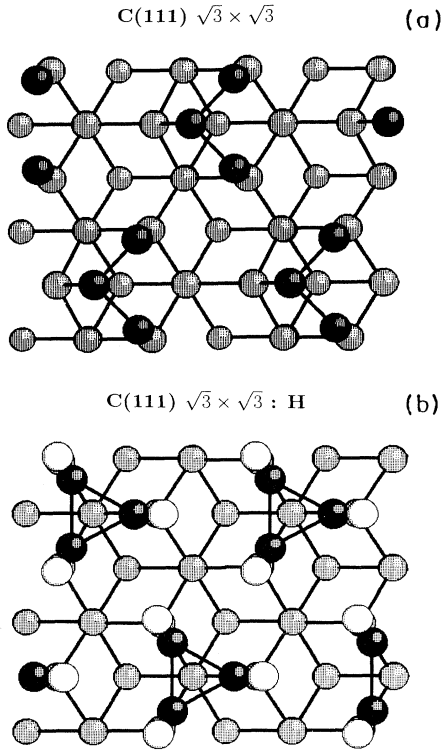

FIG. 9. Top views of the stable C(111)$\sqrt{3}\times\sqrt{3}R30°$ reconstructed surfaces: top, clean T-site and bottom, hydrogenated H-site configuration.

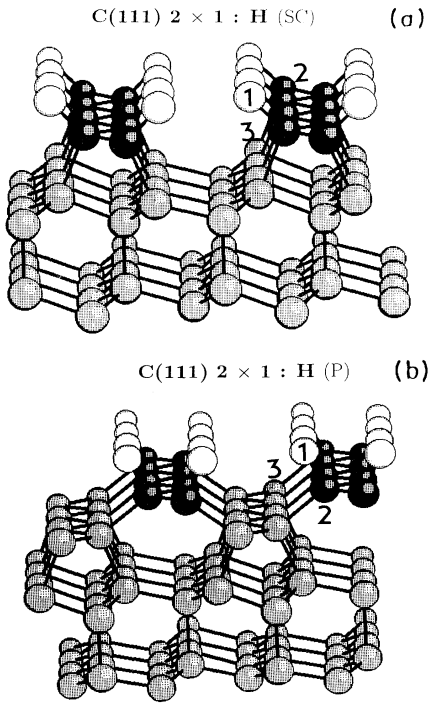

FIG. 10. Stable diamond (111) surface structures. (a) C(111)2×1:H (SC); (b) C(111)2×1:H (P).

V. ELECTRONIC SURFACE PROPERTIES

In order to characterize the electronic properties of our computationally obtained surfaces, we have calculated the LDOS at specific atoms within the surface layers. These calculations were performed by means of the Haydock recursion method[57] with usage of *ab initio* LCAO Hamiltonian and overlap parameters based on the minimal basis of atomiclike orbitals (Sec. IV). Within this method, one recursively transforms the given basis set of all atoms into a new one of orthonormal but successively more remote orbitals related to the atom in question. The Hamiltonian matrix for this basis becomes tridiagonal, and the matrix dimension needed to construct the LDOS may be confined to the elements calculated by the first recursion steps.

The LDOS projected on some chosen atomic orbital $|\varphi_\mu\rangle$,

$$n_\mu(E)=\sum_i |\langle\varphi_\mu|\psi_i\rangle|^2\delta(E-\varepsilon_i)$$

$$=-\frac{1}{\pi}\,\mathrm{Im}\langle\varphi_\mu|(E-\hat{h})^{-1}|\varphi_\mu\rangle$$

(sum over all eigenstates $|\psi_i\rangle$ with eigenvalues ε_i), is derived by setting the starting orbital of the recursion equal to $|\varphi_\mu\rangle$. Then the resulting continued fraction for the inverse matrix element was evaluated using the Gaussian quadrature approach.[58] For a sufficiently accurate DOS picture we used 30 recursion levels.

The two-dimensional periodicity of the surface structures was taken into consideration by expanding the recursion orbitals into two-dimensional Bloch states. Therefore the calculation of the new Hamiltonian matrix elements requires the integration over the two-dimensional (2D) Brillouin zone of the structures which was approximated by a special **k**-point procedure.[59,60] In our case, about 150 **k** vectors were necessary, which is determined by the length of the continued fraction. The Fermi energies E_F of the systems were obtained by calculating the total densities of states within a random-initial-vector approach[61] and integrating over all occupied states. However, in cases where a diamondlike band gap is retained, the midgap E_F of diamond was used.

A. (100) surfaces

Let us start our discussion with electronic properties of (100) surfaces. The atoms at the top of the hydrogen-free (2×1) surface possess one unbound $sp^{3.59}$ (Ref. 3.59) hybrid orbital (22% *s* character, see Table I), which gives rise to a π-like bond with the symmetrically arranged neighbor surface atom. The total bond order of this bond, calculated by us via Löwdin orthogonalized hybrid orbitals,[62] is 1.765. This value is large enough to specify this bond as a double bond, as was done using different methods by Verwoerd.[31]

The π-like character may clearly be seen from the LDOS shown in Fig. 11. The relatively weak interaction of the free hybrids yields bonding and antibonding states grouped around the Fermi energy inside the bulk-diamond gap region. These states are strongly localized

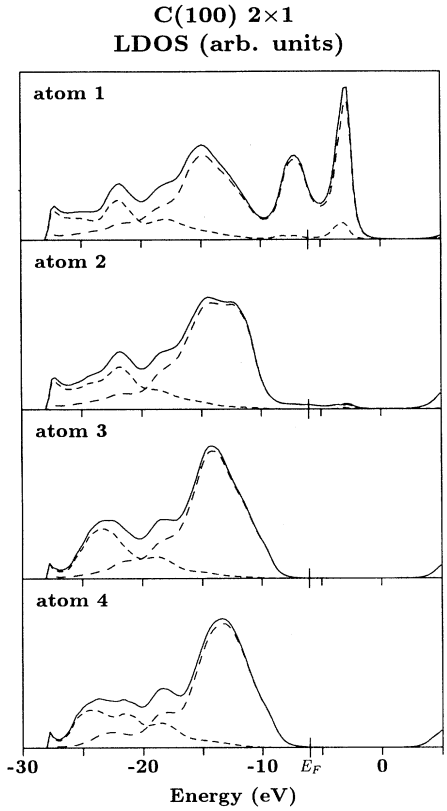

FIG. 11. Local density of electronic states (LDOS) at selected surface atoms. The atom numbers correspond to the atom numbers in Fig. 7(a) atoms 3 and 4 are located in the next deeper substrate layer. The solid and dashed line (short, long) indicate the total, the *s*, and the *p* DOS: C (100)2×1.

to the first surface layer and consequently have only minor influence on the LDOS of lower-lying atoms. Furthermore, a characteristic one-dimensional-like low valence band edge is found at all atoms, accompanied by a small lowering of this edge of about 0.5 eV on atom 2 compared to bulk diamond. This effect is ascribed to the inclined chains formed by the first and second surface-layer atoms. Along these chains, the hybrid orbitals show increased *s* orbital character, whereas the interatomic distances are decreased compared to bulk-diamond values. The interaction between these chains, indicated by the larger *p* character of the orbitals parallel to the surface, proves to be more *p*-like and affects mainly the dominating *p* peak in the surface DOS.

Going to the monohydrogenated (100)2×1:H structure, the surface atoms attain complete σ-like chemical bond saturation by also creating a dimerized state. The surface DOS picture, shown in Fig. 12, reflects this bond saturation by retaining a bulk-diamond gap at all surface atoms. The new surface bond leads, however, to a large departure from the diamond sp^3 hybridization for the orbitals forming this bond and those directed to the hydrogen atoms. Therefore changes in the LDOS from bulk diamond for the topmost atoms will be expected, diminish-

ing quickly for lower-lying atoms. Here again, we find the influence of the surface chains on the lower band edge of the LDOS, but due to the more diamondlike values in Table I this is less distinct as in the case of the clean (100)2×1 surface.

Contrary to Gavrilenko,[63] we could not find any surface states that occupy the diamond gap region for this structure. Different behavior has been found for the alternating monohydrogenated and dihydrogenated (100)1×1 surface, as shown in Fig. 13. It is very interesting to note the δ-like p peak in the gap region of the monohydrogenated surface atom. This peak correlates with the pure, unbound p orbital at this atom that points parallel to the surface. A minor influence of this p state can also be seen in the LDOS at the neighboring dihydrogenated atom. The existence of such nonbonding states should cause a strongly increased surface conductivity.

The LDOS at the hydrogen atoms differs by the fact that these atoms form bonds with differently hybridized carbon orbitals. The s content of the carbon hybrid directed to the single H neighbor is significantly higher

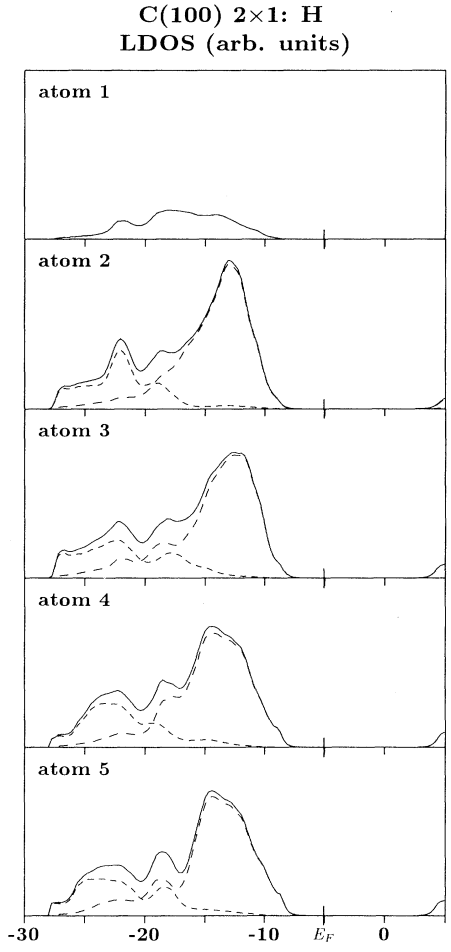

FIG. 12. LDOS: C(100)2×1:H. The atom numbers correspond to the atom numbers in Fig. 7(b); atoms 4 and 5 are located in the next deeper layer.

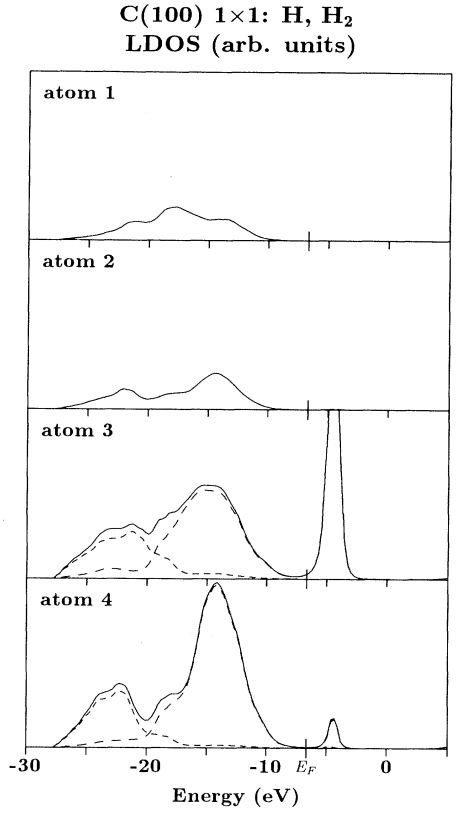

FIG. 13. LDOS C(100)1×1:H, H_2. The atom numbers correspond to the atom numbers in Fig. 7(c).

than to one of the paired hydrogens which mainly correlates with the height of the central peak in the valence hydrogen LDOS near −18 eV.

B. (111) surfaces

First we consider the (111)1×1:H surface structure. This case is less spectacular because of the maintenance of the diamond short-range order in the bond angles and C-C distances. As a consequence, the calculated DOS's are very similar to that of bulk diamond. The bond saturation by hydrogen obviously affects first of all the shape of the main p peak, which can be understood from the maximum of hydrogen s states in this energy region. The preservation of the diamond gap may also be clearly seen in Fig. 14.

Completely different DOS results have been obtained from the $(\sqrt{3}\times\sqrt{3})$ surfaces, as seen in Figs. 15 and 16. The DOS pictures at the immediate surface atoms show no similarity to bulk diamond due to the rather peculiar trimer creation. But even the lower-lying atoms still exhibit strong modifications from bulk results. A common features of all trimer atoms is the appearance of δ-like peaks in the gap region. But these emerge for different reasons. At the unhydrogenated surface the topmost atoms form some "*open trimer*" with a small angle of 94° at the vertex. This geometry, together with the downward bonds, leads to one free hybrid orbital with small s

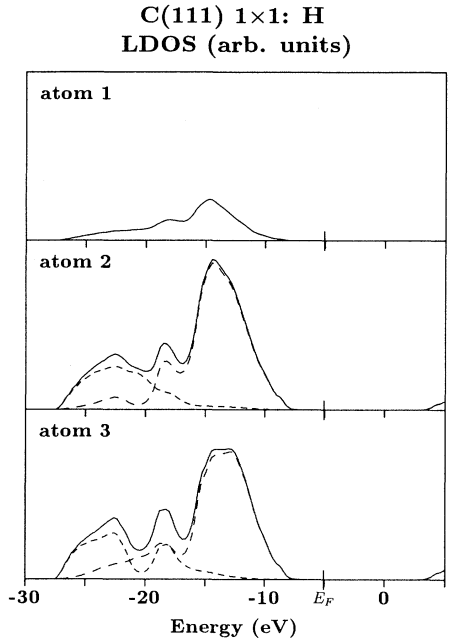

FIG. 14. LDOS C(111)1×1:H. The atom numbers correspond to the atom numbers in Fig. 8(a).

character at atom 1. The atoms 2 at the base of this isosceles triangle, however, have only two bound neighbors—a situation similar to carbene molecules. Hence the small interaction of all these free hybrids including small contributions from other neighbored atoms determine the sharp defect states seen in the LDOS picture for this structure. The Fermi energy, eventually, lies in such a high defect region from which a large, probably metallic surface conductivity may be expected.

The atoms at the (111)$\sqrt{3}\times\sqrt{3}$:H surface are formally completely chemically saturated. But the trimer is closed, leading to an equilateral triangle with 60° bond angles. Any description in terms of bond-directed orthonormal hybrids is therefore impossible. This bond arrangement is also found in cyclopropane, a molecule with reduced stability due to high bond tension. The atomic states cannot overlap strongly, consequently characteristic defect states remain in the gap region of this surface DOS. The Fermi energy lies in a small pseudogap that also entails some surface conductivity.

VI. COMPARISON BETWEEN THEORY AND EXPERIMENT, CONCLUDING REMARKS

Experimentally observed stable surface structures of diamond (100) and (111), determined by STM, are theoretically confirmed by MD simulations. The calculation of the interatomic forces is based on quantum-mechanical origin using a semiempirical DF approach. This method, currently developed for stability investigations of amorphous hydrocarbon modifications,[64] is physically motivated as well as fast and easy to use for computer simulations. The method overcomes the transferability problem from one type of structure to another one and to the incorporation of hydrogen. It includes first principles ideas, relating the chemical bonding properties to a minimal basis of localized atomic valence electron orbitals.

The investigations of the stability and restructuring dynamics of clean (100) and (111) surfaces as well as adsorbed monolayers onto these surfaces under SA conditions have been performed by the use of two-dimensional periodic thin surface slab arrangements. The theoretically determined stable and metastable surface modifications have been characterized in their statistical structure properties and chemical bonding.

When the experimentally obtained and simulated structures are compared to each other, details of the STM images on the atomic scale and of the simulations, such as bond formation and the LDOS distributions, are opposed to each other. Both Figs. 1 and 2 show a C(100)2×1 surface, where individual dimers are only visible in the latter. By changing the potential drop across the tunneling gap, we were unable to make visible

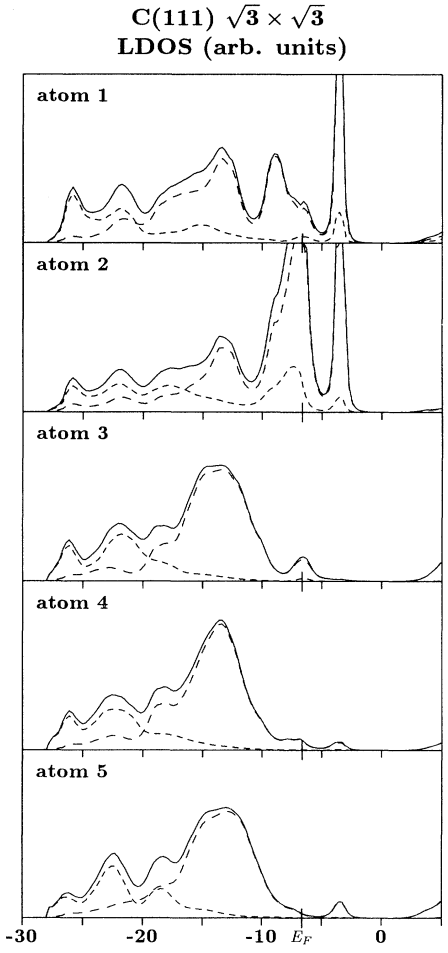

FIG. 15. LDOS C(111)$\sqrt{3}\times\sqrt{3}$. The atom numbers correspond to the atom numbers in Fig. 8(b); atom 5 is located in the next deeper layer.

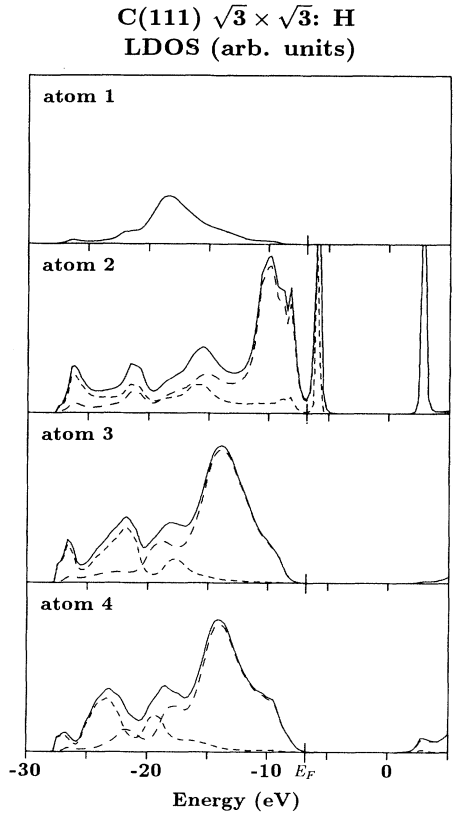

FIG. 16. LDOS C(111)$\sqrt{3}\times\sqrt{3}$:H. The atom numbers correspond to the atom numbers in Fig. 8(c); atom 4 is located in the next deeper layer.

individual dimers within the rows shown in Fig. 1, or to obtain unstructured rows in the case of Fig. 2. Consequently, the differences between the patterns visible in Figs. 1 and 2 are attributed to different atomic structures. The LDOS of the nonhydrogenated C(100)2×1 structure exhibits strong π states at the Fermi energy, whereas the C(100)2×1:H structure does not. Since the π states form delocalized metallic surface bands, it is straightforward to assign the surface shown in Fig. 1 to the nonhydrogenated and that of Fig. 2 to the hydrogenated structure.

From the MD simulations, the (111) faces show (1×1), (2×1), and ($\sqrt{3}\times\sqrt{3}$)R30° structures. Experimentally, the (1×1) and ($\sqrt{3}\times\sqrt{3}$)R30° structures are clearly visible in the STM images. Though we do not have direct evidence for the (2×1) structures, the rows visible in Fig. 4 would be due to the Pandey chain structure in case the STM does not distinguish between the upper and lower rows (as it is quite possible because of its very similar chemical bonding properties).

The calculations have unequivocally shown that the (111)1×1 and (111)$\sqrt{3}\times\sqrt{3}R$30° structures can only be attributed to the 1DB and 3DB surfaces, respectively. Thus 1DB as well as 3DB surfaces are visible on (111) faces as they have grown, which gives strong evidence that the two different single atomic layers grew alternating and not simultaneously. The fine structure within a trimer, clearly visible in the center of Fig. 3, allows its assignment to the nonhydrogenated structure, where the *"open trimers"* are located at the H sites.

By relating the stable surface modifications and properties determined by MD to STM measurements some inferences on sequential growth steps are given. The stable surface modifications in a next MD simulation step may act as substrate layers for thermal adsorption studies of C and H atoms, radicals or molecules. Via the stable adsorbate configurations, the energetically most favorable pathways for diamond growth may be analyzed and conditions may be determined for stabilizing them.

Furthermore, by closely relating detailed surface sensitive high resolution results from experiments performed *in situ,* e.g., ultraviolet photoelectron spectroscopy (UPS), LEED, electron energy loss spectroscopy (EELS), and attenuated total reflection infrared spectroscopy (ATR-IR) to theoretical investigations of vibrational and electronic surface DOS for different surface structures and adsorbate configurations a more fundamental understanding of growth mechanisms will be achieved on the molecular level of chemical bonding.

ACKNOWLEDGMENTS

We gratefully acknowledge the support from the Deutsche Forschungsgemeinschaft under Contract Nos. Fr 889/4-1, Fr 889/6-1, and Bu 781/1-1.

[1]B. V. Spitsyn, L. L. Bouilov, and B. V. Derjaguin, Cryst. Growth **52**, 219 (1981).
[2]S. Matsumoto, Y. Sato, M. Kamo, and N. Setaka, Jpn. J. Appl. Phys. **21**, L183 (1982).
[3]R. C. De Vries, Annu. Rev. Mater. Sci. **17**, 161 (1987).
[4]J. C. Angus and C. C. Hayman, Science **241**, 913 (1988).
[5]K. E. Spear, J. Am. Ceram. Soc. **72**, 171 (1989).
[6]Y. Yarbrough and R. Messier, Science **247**, 688 (1990).
[7]M. Frenklach and K. E. Spear, J. Mater. Res. **3**, 133 (1988).
[8]T. R. Anthony, in *Diamond, Silicon Carbide and Related Wide Bandgap Semiconductors,* edited by J. T. Glass, R. F. Messier, and N. Fujimori, MRS Symposia Proceedings No. 162 (Materials Research Society, Pittsburgh, 1990), p. 61.
[9]S. J. Harris and A. M. Weiner, J. Appl. Phys. **67**, 6520 (1990).
[10]S. J. Harris, Appl. Phys. Lett. **56**, 2298 (1990).
[11]S. P. Mehandru and A. B. Anderson, Surf. Sci. **248**, 369 (1991).
[12]P. Deak, J. Giber, and H. Oechsner, Surf. Sci. **250**, 287 (1992).
[13]B. J. Garrison, E. J. Dawnkaski, D. Srivastava, and D. W. Brenner, Science **255**, 835 (1992); D. W. Brenner, Phys. Rev. B **42**, 9458 (1990).
[14]X. G. Zhao, C. S. Carmer, B. Weiner, and M. Frenklach, J. Phys. Chem **97**, 1639 (1993).
[15]Th. Frauenheim and P. Blaudeck, Appl. Surf. Sci. **60/61**, 281

(1992).
[16]P. M. Agrawal, D. L. Thompson, and L. M. Raff, Surf. Sci. **195**, 283 (1988); J. Chem. Phys. **91**, 5021 (1989).
[17]D. W. Brenner, B. I. Dunlap, J. W. Mintmire, R. C. Mowrey, and C. T. White, in *Proceedings of the 2nd International Symposium on Diamond Materials,* edited by A. J. Purdes *et al.* (The Electrochemical Society, Pennington, NJ, 1991), p. 39.
[18]B. A. Pailthorpe, J. Appl. Phys. **70**, 543 (1991).
[19]P. C. Weakliem and E. A. Carter, J. Chem. Phys. **96**, 3240 (1992).
[20]S. Iarlori, G. Galli, F. Gygi, M. Parinello, and E. Tosatti, Phys. Rev. Lett. **69**, 2947 (1992).
[21]J. Tersoff, Phys. Rev. Lett. **56**, 632 (1986); Phys. Rev. B **37**, 6991 (1988); Phys. Rev. Lett. **61**, 2879 (1988).
[22]D. W. Brenner, Phys. Rev. B **42**, 9458 (1990).
[23]W. Andreoni and G. Pastore, Phys. Rev. B **41**, 10 243 (1990).
[24]Th. Frauenheim and J. Widany (unpublished).
[25]M. R. Pederson, B. M. Klein, and J. Q. Broughton, Phys. Rev. B **38**, 3825 (1988).
[26]K. Nath and A. B. Anderson, Solid State Commun. **66**, 277 (1988).
[27]M. J. S. Dewar and W. Thiel, J. Am. Chem. Soc. **99**, 4899 (1977).
[28]P. Badziag and W. S. Verwoerd, Surf. Sci. **183**, 469 (1987).
[29]X. M. Zheng and P. V. Smith, Surf. Sci. **256**, 1 (1991).
[30]X. M. Zheng and P. V. Smith, Surf. Sci. **261**, 394 (1992).
[31]W. S. Verwoerd, Surf. Sci. **103**, 404 (1981); **108**, 153 (1981).
[32]M. R. Pederson, K. A. Jackson, and W. E. Pickett, Phys. Rev. B **44**, 3891 (1991).
[33]R. E. Thomas, R. A. Rudder, R. J. Markunas, D. Huang, and M. Frenklach, J. Chem. Vap. Dep. **1**, 6 (1992).
[34]M. Tsuda, N. Nakajima, and S. Oikawa, J. Am. Chem. Soc. **108**, 5780 (1986).
[35]K. C. Pandey, Phys. Rev. B **25**, 4338 (1982).
[36]G. Seifert, H. Eschrig, and W. Biegert, Z. Phys. Chem. (Leipzig) **267**, 529 (1986).
[37]D. A. Drabold, R. Wang, and S. Klemm, Phys. Rev. B **43**, 5132 (1991).
[38]P. Blaudeck, Th. Frauenheim, D. Porezag, G. Seifert, and E. Fromm, J. Phys. Condens. Matter **4**, 6389 (1992).
[39]S. H. Yang, D. A. Drabold, and J. B. Adams, Phys. Rev. B **48**, 5261 (1993).
[40]H.-G. Busmann, H. Sprang, I. V. Hertel, W. Zimmermann-Edling, and H.-J Güntherodt, Appl. Phys. Lett. **59**, 295 (1991).
[41]H. Sprang, S. Lauer, H.-G. Busmann, and I. V. Hertel, Appl. Phys. A **55**, 347 (1992).
[42]H.-G. Busmann, W. Zimmermann-Edling, H. Sprang, H.-J. Güntherodt, and I. V. Hertel, Diamond Relat. Mater. **1**, 979 (1992).
[43]H.-G. Busmann, W. Zimmermann-Edling, S. Lauer, Th. Frauenheim, P. Blaudeck, and D. Porezag, Surf. Sci. **295**, 340 (1993).
[44]W. Zimmermann-Edling, H-G. Busmann, H. Sprang, and I. V. Hertel, Proc. STM91, Interlaken, Swiss, Ultramicroscopy **42**, 1366 (1992).
[45]T. Tsuno, T. Imai, Y. Nishivayashi, K. Hamada, and F. Fujimori, Jpn. J. Appl. Phys. **30**, 1063 (1991).
[46]D. J. Chadi, Phys. Rev. Lett. **43**, 43 (1979).
[47]J. E. Northrup, Phys. Rev. Lett. **53**, 683 (1984).
[48]D. J. Chadi, Ultramicroscopy **31**, 1 (1989).
[49]L. Hedin and B. I. Lundquist, J. Phys. C **4**, 2064 (1971).
[50]G. Seifert and H. Eschrig, Phys. Status Solidi B **127**, 573 (1985).
[51]J. E. Inglesfield, Mol. Phys. **37**, 879 (1975).
[52]D. Tomanek and M. A. Schluter, Phys. Rev. B **36**, 1208 (1987).
[53]G. Seifert and R. O. Jones, Z. Phys. D **20**, 77 (1991).
[54]L. Verlet, Phys. Rev. **159**, 98 (1967).
[55]A. V. Hamza, G. D. Kubiak, and R. H. Stulen, Surf. Sci. **237**, 35 (1990).
[56]Y. L. Yany and M. P. D'Evelyn, J. Am. Chem. Soc. **114**, 2796 (1992); J. Vac. Sci. Technol. A **10**, 978 (1992).
[57]V. Heine, D. W. Bullett, R. Haydock, and M. J. Kelly, in *Solid State Physics: Advances in Research and Applications,* edited by F. Seitz, D. Turnbull, and H. Ehrenreich (Academic, New York, 1980), Vol. 35.
[58]C. M. M. Nex, J. Phys. A **11**, 653 (1978).
[59]H. J. Monkhorst and J. D. Pack, Phys. Rev. B **13**, 5188 (1976).
[60]S. M. Anlage and D. L. Smith, Phys. Rev. B **34**, 2336 (1986).
[61]M. Krajči, J. Phys. F **17**, 2217 (1987).
[62]E. R. Davidson, J. Chem. Phys. **46**, 3320 (1967).
[63]V. I. Gavrilenko, Phys. Rev. B **47**, 9556 (1993).
[64]P. Blaudeck, Th. Frauenheim, G. Jungnickel, and U. Stephan, Solid State Commun. **85**, 992 (1993).

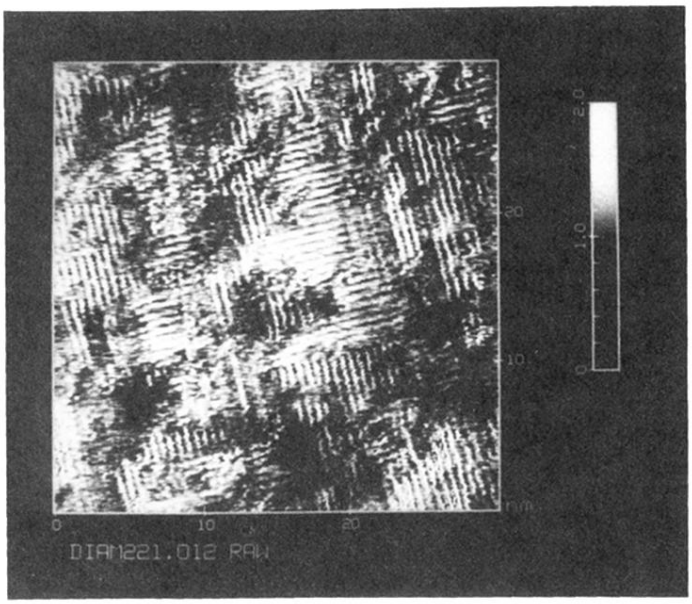

FIG. 1. Image of a (100) facet of a polycrystalline diamond film obtained with a scanning tunneling microscope. Deposition parameters: 1 mol % CH_4 in H_2, substrate temperature equals 925 °C, continuous accelerated beam for gas inlet (Ref. 43), diameter of orifice equals 20 μm, stagnation pressure behind the nozzle equals 6 bars, temperature of the nozzle equals 500 °C, gas flow equals 22 SCCM, pressure in the chamber equals 50 mbar. Tunneling parameters: constant height mode, $I_t = -1.0$ nA, $U_t = -183$ mV.

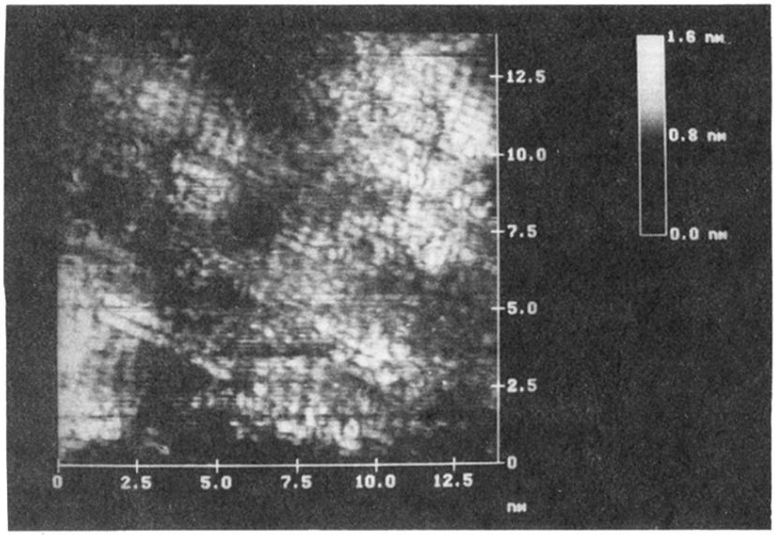

FIG. 2. Image of a (100) facet of a polycrystalline diamond film obtained with a scanning tunneling microscope. Deposition parameters: 1 mol% CH_4 in H_2, substrate temperature equals 925 °C, continuous accelerated beam for gas inlet, diameter of orifice equals 30 μm, stagnation pressure behind the nozzle equals 1.5 bars, temperature of the nozzle equals 950 °C, gas flow equals 30 SCCM, pressure in the chamber equals 50 mbar. Tunneling parameters: constant height mode, $I_t = -1.7$ nA, $U_t = 400$ mV.

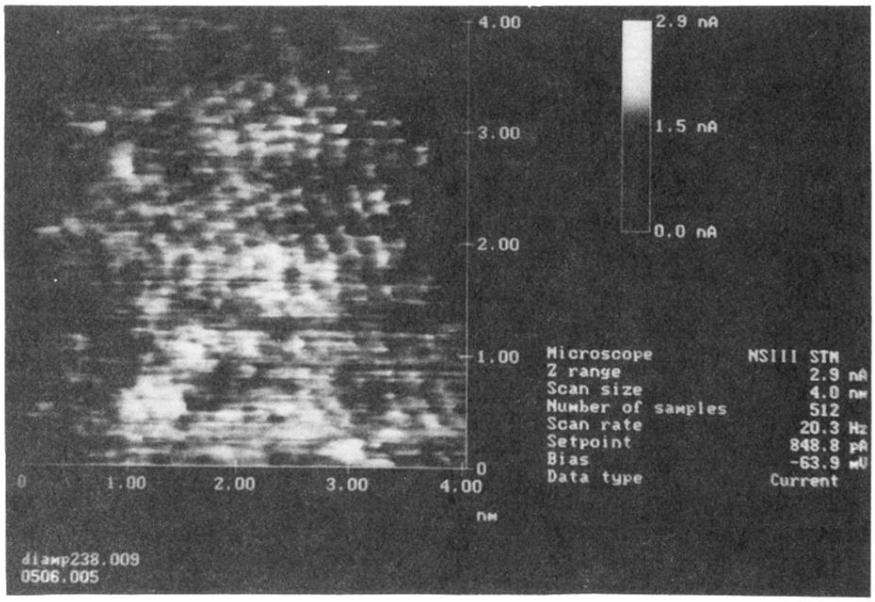

FIG. 3. Image of a (111) facet of a polycrystalline diamond film obtained with a scanning tunneling microscope. The deposition parameters are the same as those for the film of Fig. 2. Tunneling parameters: constant current mode, $I_t = 0.85$ nA, $U_t = -64$ mV.

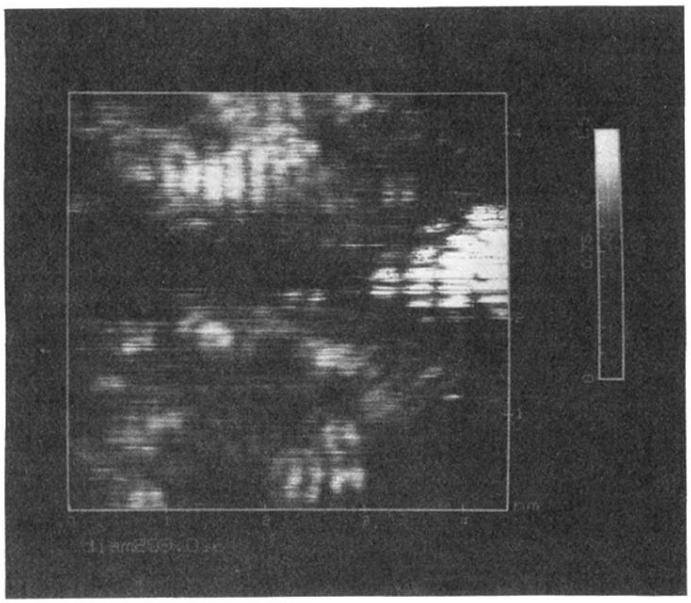

FIG. 4. Image of a (111) facet of a polycrystalline diamond film obtained with a scanning tunneling microscope. Deposition paramers: 1 mol % CH_4 in H_2, substrate temperature equals 925 °C, pulsed accelerated beam for gas inlet (Ref. 41), stagnation pressure behind the nozzle equals 1.5 bars, temperature of the nozzle is RT, averaged gas flow equals 75 SCCM, background pressure in the chamber equals 50 mbar. Tunneling parameters: constant current mode, $I_t = 1.3$ nA, $U_t = 574$ mV.

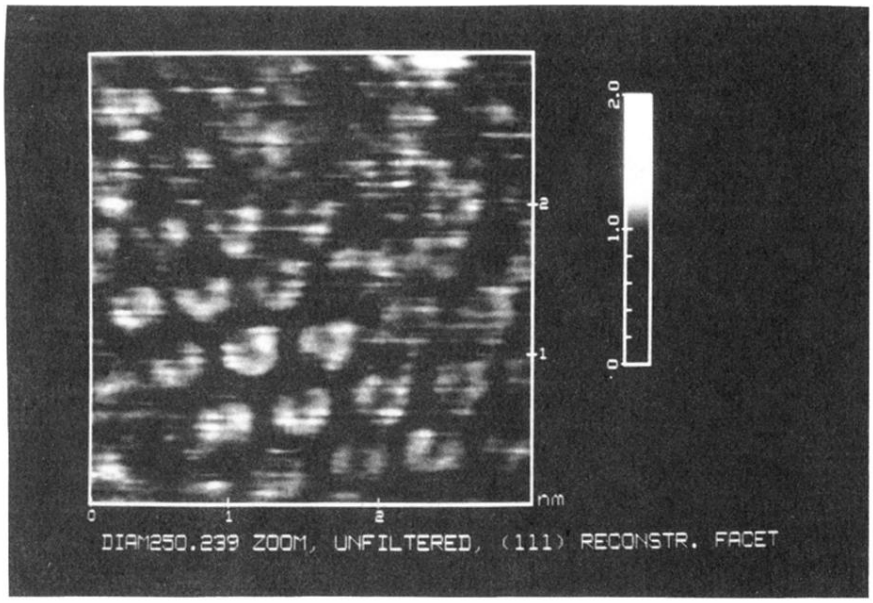

FIG. 5. Image of a (111) facet of a polycrystalline diamond film obtained with a scanning tunneling microscope. The deposition parameters are the same as those for the film of Fig. 2. Tunneling parameters: constant current mode, $I_t = 0.5$ nA, $U_t = -48$ mV.

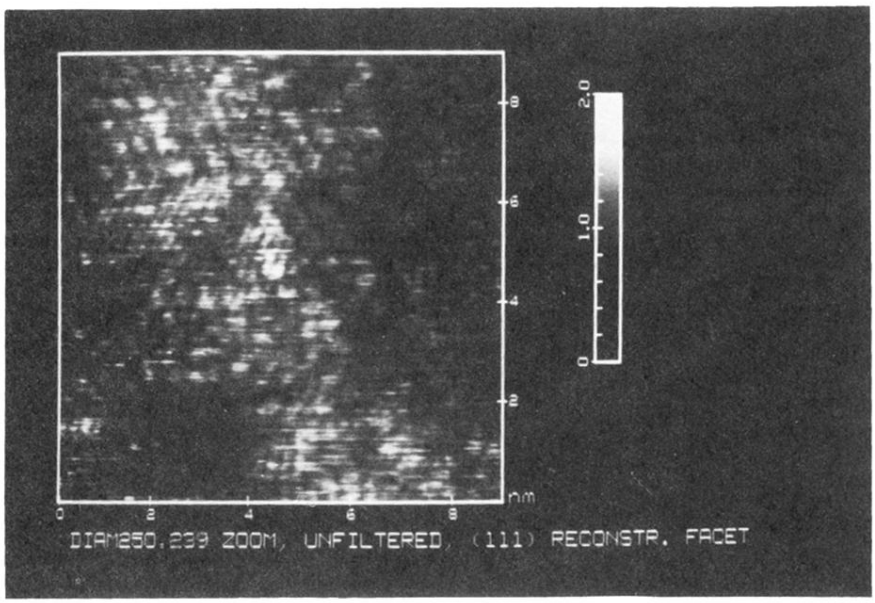

FIG. 6. Image of a (111) facet of a polycrystalline diamond film obtained with a scanning tunneling microscope. The deposition parameters are the same as those for the film of Fig. 2. Tunneling parameters: constant current mode, $I_t = -0.5$ nA, $U_t = -48$ mV.